



Article

Novel Blue-Wavelength-Blocking Contact Lens with Er³⁺/TiO₂ NPs: Manufacture and Characterization

Lina Mohammed Shaker ¹, Ahmed Alamiery ^{1,2,*} , Mohd Takriff ^{1,3} and Wan Nor Roslam Wan Isahak ¹

¹ Department of Chemical and Process Engineering, Faculty of Engineering and Built Environment, Universiti Kebangsaan Malaysia (UKM), Bangi 43000, Selangor, Malaysia; wannorroslam@ukm.edu.my (L.M.S.); sobritakriff@ukm.edu.my (M.T.); p109960@siswa.ukm.edu.my (W.N.R.W.I.)

² Energy and Renewable Energies Technology Center, University of Technology, Baghdad 10001, Iraq

³ Chemical and Water Desalination Engineering Program, Collage of Engineering, University of Sharjah, Sharjah 26666, United Arab Emirates

* Correspondence: dr.ahmed1975@gmail.com or dr.ahmed1975@ukm.edu.my

Abstract: Thermally stable titanium dioxide nanoparticles (TiO₂ NPs) doped with erbium ions (Er³⁺) are characterized by uniformity, low excitation energy, and high surface area. The impregnation methodology was used to enhance the optical properties of TiO₂ NPs impregnated with various Er³⁺ ion contents. The synthesized Er³⁺/TiO₂ samples were characterized by energy dispersive X-ray (EDX), metal mapping, UV-Visible spectrum, field emission scanning electron microscopy (FESEM), and X-ray diffraction (XRD). The Er³⁺ ions, per our findings, were well-distributed on the TiO₂ surface of the anatase phase and there was an insignificant difference in particle size, but there was no change in the particle shapes of the Er³⁺/TiO₂ NPs structure. The maximum band gap degradation occurred with 1.8 wt % of Er³⁺/TiO₂, where the energy gap degraded from 3.13 to 2.63 eV for intrinsic TiO₂. The synthesized Er³⁺/TiO₂ samples possess predominantly finely dispersed erbium ion species on the surface. Er³⁺ ions agglomeration on the surface increased with increasing ions in each sample. We found that 0.6 wt/vol % of Er³⁺/TiO₂ is the best optical coating and produced satisfying results in terms of blocking the transmittance of blue wavelength without reducing the image quality.

Keywords: titanium dioxide; erbium ions; high surface area; impregnation method; optical characteristics



Citation: Shaker, L.M.; Alamiery, A.; Takriff, M.; Wan Isahak, W.N.R. Novel Blue-Wavelength-Blocking Contact Lens with Er³⁺/TiO₂ NPs:

Manufacture and Characterization. *Nanomaterials* **2021**, *11*, 2190. <https://doi.org/10.3390/nano11092190>

Academic Editor: Shin-Tson Wu

Received: 30 July 2021

Accepted: 18 August 2021

Published: 26 August 2021

Publisher's Note: MDPI stays neutral with regard to jurisdictional claims in published maps and institutional affiliations.



Copyright: © 2021 by the authors. Licensee MDPI, Basel, Switzerland. This article is an open access article distributed under the terms and conditions of the Creative Commons Attribution (CC BY) license (<https://creativecommons.org/licenses/by/4.0/>).

1. Introduction

Recently, various methods have been studied and applied for modifying mineral surfaces [1,2]. Such methods enhance the activity of titanium dioxide (TiO₂) for different applications [3], for example, as a photocatalyst for the photocatalytic degradation (PCD) of pollutants [4], both organic and inorganic [5,6], and for sterilizing wastewater [7]. A photocatalytic antimicrobial film was coated on a polymeric contact lens surface to fabricate an anti-contamination contact lens and other applications [8]. Hybrid poly(methyl methacrylate-dioxide) systems have been widely reported, focusing mostly on PMMA-SiO₂ [9], PMMA-TiO₂ [10], and PMMA-ZrO₂ [11]; these nanocomposites are used in the fabrication of optical and biomedical devices such as contact lenses [11]. Nanocomposite polymers have attracted significant attention in optical applications because of their enhanced optical performance. Recently, nanoparticles (NPs) such as TiO₂, ZnO, ZnS, ZrO₂, and so forth, have been exploited to obtain a high refractive index (*n*) and low dispersion nanocomposite [12,13]. Switchable wettability materials such as TiO₂-based polymers are considered good photocatalytic coating candidates able to block the undesired ultraviolet (UV) spectrum [14].

The TiO₂ photocatalyst is characterized by its ease of synthesis, low cost, nontoxicity, high stability, high band-gap energy (3.2 eV) [15], and applicability for PCD [16]. Despite these qualities, it is now of little use in large-scale processing operations due to its low

quantum efficiency and short wavelength excitation. According to the concept of irradiation, when the particles are irradiated with near ultraviolet rays of energy greater than or equal to 350 nm [17], the electrons migrate from the valence band to reach the conduction band (e_{cb}^-) leaving behind positive holes (h_{vb}^+), where they initiate oxidation reactions and reduction reactions with the absorbed species [18]. Such charges can be recombined to generate an e^- -hole pair that is not available to participate in the required reactions. Before this process takes place, oxidation and reduction processes occur by means of electrons and holes, which control the efficiency of the photocatalytic TiO_2 -catalyzed reaction [19,20].

One of the approaches that has been widely adopted to improve the photocatalytic efficiency of the TiO_2 photocatalyst under UV and visible light is the doping/deposition of a minute amount of a suitable metal in TiO_2 , which enhances the participation of the photogenerated holes and electrons in the photocatalytic reactions [21–25]. It was suggested that the precipitated or doped metal in TiO_2 has high Schottky barriers in the metal- TiO_2 contact area and thus acts as an electronic trap, which facilitates the separation of the electron hole and enhances the electron transfer process of the interface, thus enhancing the photocatalyst's efficiency [26]. According to the higher energy gap of TiO_2 NPs, one way to make these particles useful in terms of photocatalytic activity is by doping the TiO_2 NPs with rare earth ions, where these ions decrease the metal oxide band gap [27]. Visible light represents about 43% of the solar spectrum, so researchers have aimed to improve the absorption of visible light by TiO_2 due to its previously mentioned properties and applications in the visible and ultraviolet frequency ranges [28–30].

This article attempts to explain and develop the existence of erbium ions with optimum quantities and their role in the physicochemical properties of the doped TiO_2 materials, especially when used as a coating filter. The best optical characteristics were obtained by the prepared nanocomposites by designing a coating layer on a contact lens front surface to fabricate a blue-blocking contact lens. In the continuation of our work [31–35] on nanomaterials, herein, we report the synthesis of TiO_2 NPs and Er^{3+}/TiO_2 by the impregnation method [36–38].

2. Materials and Methods

The chemicals erbium (III), TiO_2 NPs powder, and chloroxylenol were purchased from Sigma Aldrich (St. Louis, MO, USA) and utilized without further purifications. The Er^{3+} contained acetylacetonate hydrate, was CAS grade, and had a purity of 97%. The TiO_2 nanopowder had 99.5% purity and a 21 nm diameter according to the TEM from Philips (Eindhoven, The Netherlands), and the chloroxylenol had 98% purity. The chloroxylenol was prepared, and deionized water was used for this purpose as well as for dilution.

2.1. Er^{3+}/TiO_2 Preparation

TiO_2 NPs was impregnated with Er^{3+} ions with 0.6, 1.2, 1.8, and 2.4 wt % using an 80 mL glass beaker. We used a 10 mL of deionized water to dissolve 60, 120, 180, and 240 mg of Er^{3+} acetylacetonate hydrate, which was sonicated for 10 min. Then, each solution was added dropwise to the TiO_2 nanopowder, well-mixed with a glass rod, and stirred for 2 h at 1300 rpm. The drying process was carried out at 80 °C overnight and then calcination was performed at 500 °C for two hours.

2.2. Er^{3+}/TiO_2 Characterization

The estimation of Er^{3+}/TiO_2 NPs phase and size was achieved using D8 Advance Bruker AXS X-ray patterns (Bruker, Am Studio 2D, Berlin, Germany). Energy-dispersive X-ray (EDX), with higher resolution, was applied to investigate the synthesized NPs' morphological features using field emission scanning electron microscopy (FESEM) (SuPRA 55 VP, Carl Zeiss AG, Oberkochen, Germany). The other two analysis devices were used to characterize the NP samples were an OXFORD Penta FETx3 for metal mapping (Carl Zesis AG, Oberkochen, Germany) and a Perkin Elmer UV-Vis spectrophotometer (Waltham, MA,

USA). The intensity transmission curve of the designed coated contact lens was recorded by ZEMAX software.

2.3. Contact Lens Modeling

To design and fabricate an anti-contamination blue wavelength blocker contact lens, the UV–Vis spectral data for all the synthesized films were compared; the best n value nanocomposite was selected for coating the contact lens. The human eye optical parameters and the coated contact lens at a 5 degrees field of view under white light illumination were entered into ZEMAX software (Version 14, serial number 34,900). The two corneal surfaces (anterior and posterior cornea) were selected as aspherical surfaces (programmatically named the standard surface). The standard surface requires two specific parameters: radius and conic constant. The pupil aperture surface was selected as the stop aperture and nasally decentered by 0.5 mm with respect to the visual axis; the crystalline lens is represented by two homogeneous gradient index shells whose n value is described by:

$$n = n_0 + n_{r2}r^2 + n_{r4}r^4 + n_{r6}r^6 + n_{z1}z + n_{z2}z^2 + n_{z3}z^3 \quad (1)$$

$$r^2 = x^2 + y^2 \quad (2)$$

Both the vitreous body of the eye and the retinal imaging surface were selected as standard surfaces. The standard surface position is centered on the optical axis and its vertex located at the Z axis. The z value (sag) of the standard surface is given by:

$$z = \frac{c r^2}{1 + \sqrt{1 - (1 + k c^2 r^2)}} \quad (3)$$

where c is the curvature (reciprocal of the radius), r is the radial coordinate in the lens unit, and k refers to the conic constant.

In this work, a coating of aspheric surface of the modeled contact lens (0.12 mm thickness, 0.035 conic, and 7.748 mm and 7.8 mm radius of front and back surfaces, respectively) was constructed by an extended polynomial surface. The aspherical surface sag is defined by:

$$z = \frac{c r^2}{1 + \sqrt{1 - (1 + k) c^2 r^2}} + \sum_{i=1}^N A_i E_i(x, y) \quad (4)$$

where N represents the polynomial coefficient number in the series and A_i is the coefficient on the i th extended polynomial (E) term

3. Results

3.1. X-ray Diffraction Pattern

The synthesized specimens were analyzed by XRD in order to study the crystallinity of the erbium ions/titanium dioxide ($\text{Er}^{3+}/\text{TiO}_2$) NPs and to evaluate the changes, if any, that may occur through the impregnation of TiO_2 NPs with Er ions. The X-ray diffraction scanning of the $\text{Er}^{3+}/\text{TiO}_2$ NPs is demonstrated in Figure 1. The signals of the TiO_2 types, which are anatase and rutile [37,38], were clear. These patterns demonstrate that the phase composition and the structure of the TiO_2 NPs did not change even after impregnation with Er ions. Additionally, the decrease in the intensity of the TiO_2 's peaks indicated that the crystal structure of the titanium dioxide was impregnated with Er ions.

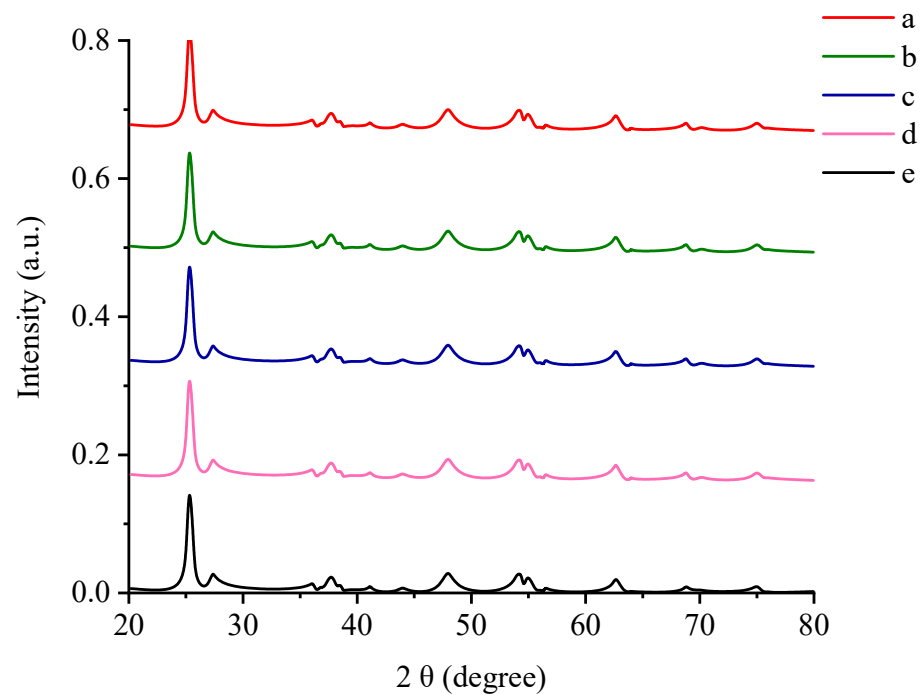


Figure 1. XRD: (a) titanium dioxide; (b) 0.6 wt %; (c) 1.2 wt %; (d) 1.8 wt %; (e) 2.4 wt % erbium ions/titanium dioxide.

Table 1 demonstrates the intensity values of the signals. The diffraction spectra of the *Er* ions/ TiO_2 NPs do not support the existence of *Er* ions. This conclusion can most probably be ascribed to the appropriate dispersion of erbium ions in the lattice structure of TiO_2 [39].

Table 1. Erbium ions/titanium dioxide intensity signals.

2θ	Intensity				
	TiO_2	0.6 wt % $\text{Er}^{3+}/\text{TiO}_2$	1.2 wt % $\text{Er}^{3+}/\text{TiO}_2$	1.8 wt % $\text{Er}^{3+}/\text{TiO}_2$	2.4 wt % $\text{Er}^{3+}/\text{TiO}_2$
25.2712	2158	1984	1911	1879	1855
27.4136	515	498	493	481	474
37.3038	127	105	100	90	90
48.0908	555	536	481	478	473
53.8206	311	310	288	262	230
53.97	379	368	351	346	336
55.116	367	340	313	291	283
62.7142	292	285	272	249	241
68.8675	165	149	143	131	120
70.2128	145	114	109	108	104
75.0956	185	164	163	151	147

The crystallite size data are listed in Table 2 for TiO_2 with *Er* ions in weight percent [15]. The lesser increase in the size of the particles confirmed that impregnation increased for the *Er* ions/ TiO_2 NPs sample. The Debye–Scherer equation is used to calculate the crystallite size *D* (Equation (5)):

$$D = \frac{K\lambda}{\beta \cos \theta} \quad (5)$$

where the Scherer constant (*K*) is equal to 0.89, λ is the wavelength, β is the width of the peak, and θ is the angle of Bragg diffraction.

Table 2. Size of crystallite particles of all synthesized samples.

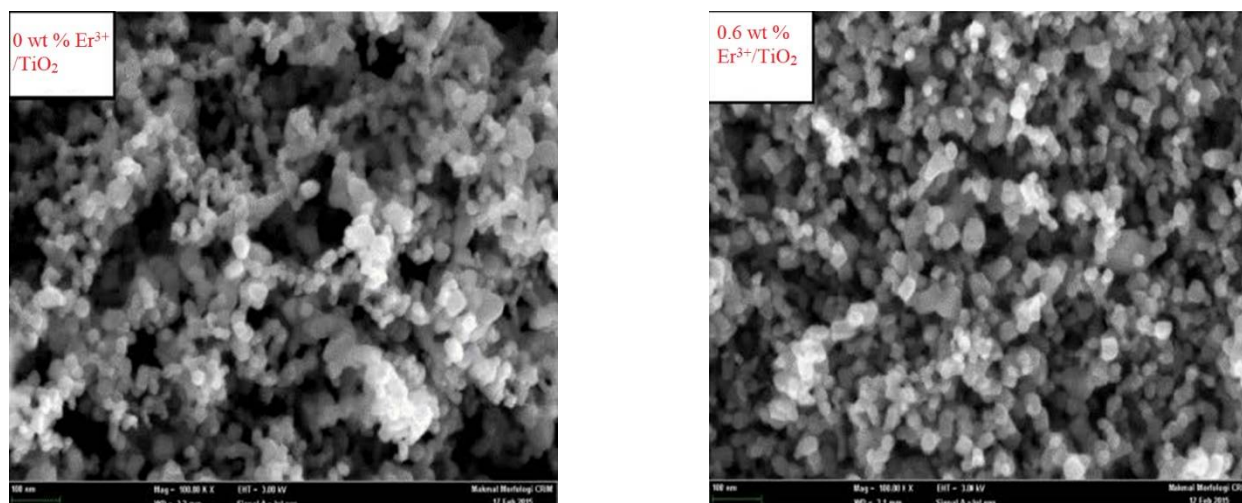
Er ³⁺ /TiO ₂ (wt %)	Crystallite (nm)
TiO ₂	28.72
0.6	28.84
1.2	31.53
1.8	33.93
2.4	35.93

3.2. Surface Morphology

The Er³⁺/TiO₂ NPs surface morphologies were examined utilizing FESEM and EDX in addition to metal mapping. The FESEM images are demonstrated in Figure 2. The images of the Er³⁺/TiO₂ sample demonstrate the particles' shapes, which showed less agglomeration and were generally spherical. EDX analysis was performed on the Er³⁺/TiO₂ samples to study the presence of *Er* ions on the surfaces of the examined TiO₂. The results of EDX spectra analysis are provided in Figure 3, which demonstrates that the *Er* ions were present in all investigated samples. In addition, the EDX analysis spectral results of the different weight percentages of the *Er* content in the tested samples are listed in Table 3. The theoretical and empirical *Er* contents show considerable agreement. Metal mapping tests were performed to study the *Er* ions' dispersion on the surface of the TiO₂ NPs. These data are summarized in Figure 4, which reveals a considerable distribution of *Er* ions on the TiO₂ NPs in all synthesized samples.

Table 3. EDX analysis of the theoretical and empirical values of the synthesized samples.

Er ³⁺ /TiO ₂ (wt %)	Calculated Metal (wt %)	Actual Metal (wt %) by EDX
0.6	0.6	0.72
1.2	1.2	1.31
1.8	1.8	2.06
2.4	2.4	2.45

**Figure 2.** Cont.

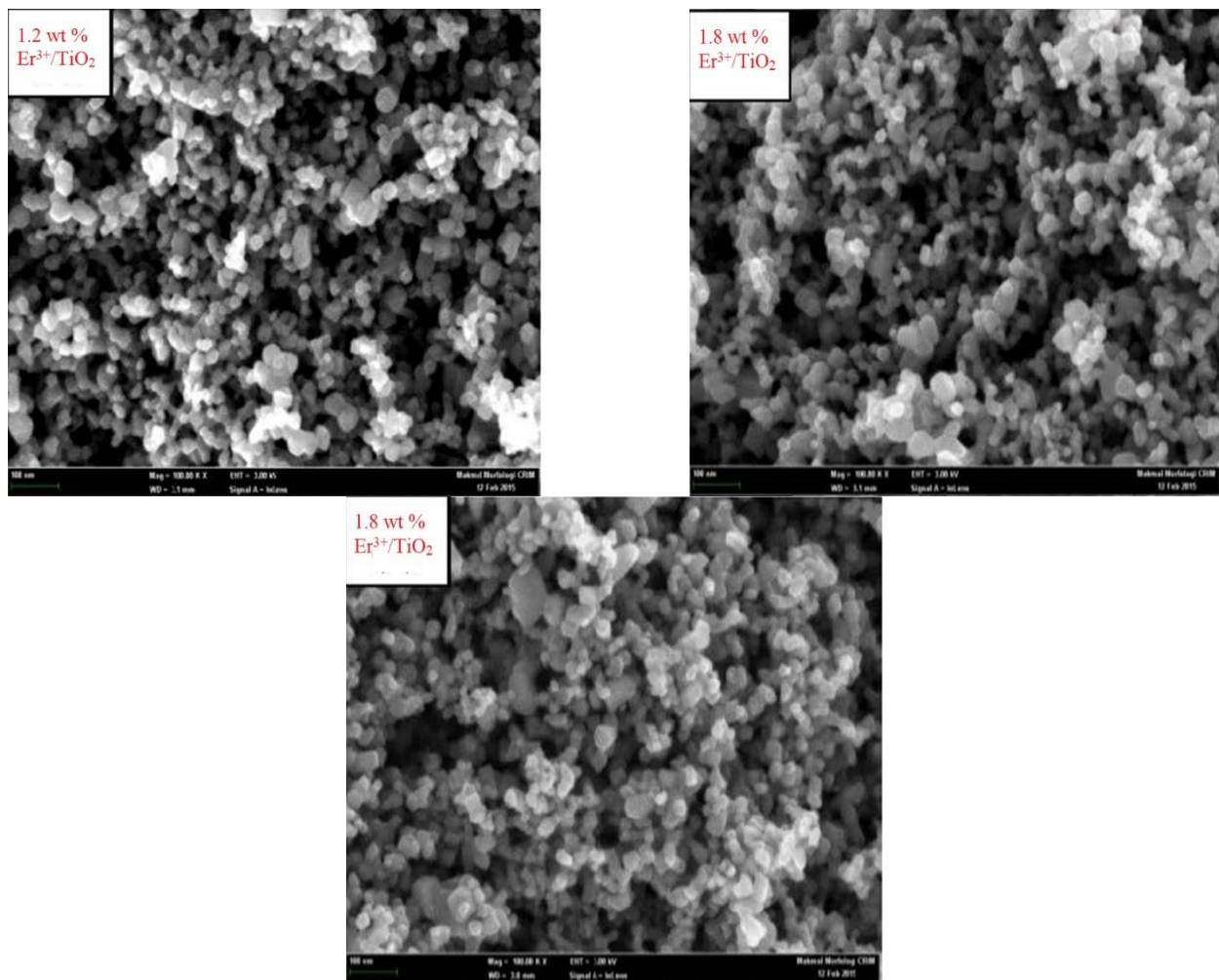


Figure 2. FESEM micrographs for the synthesized samples.

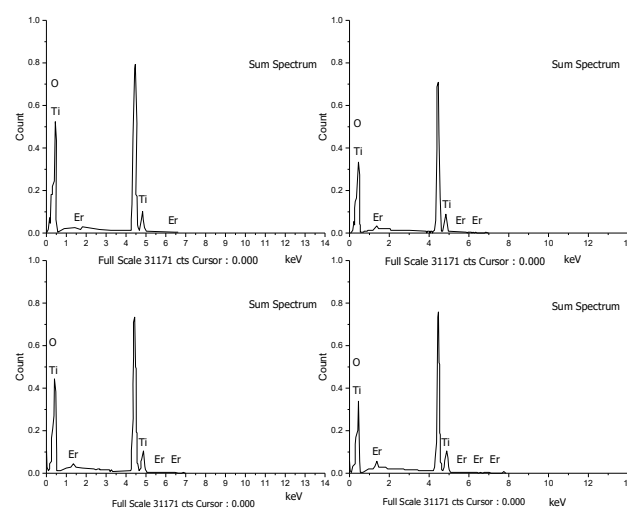


Figure 3. EDX micrographs of the synthesized samples.

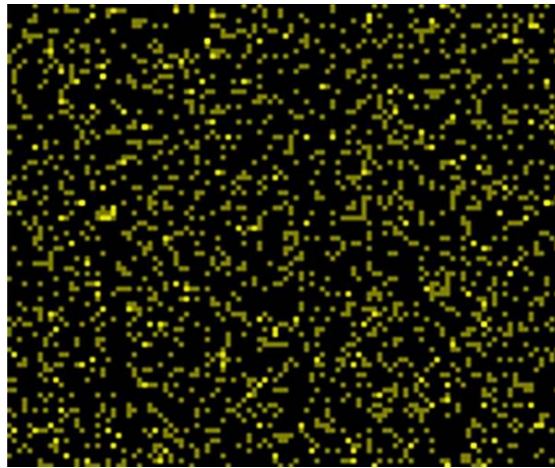


Figure 4. Metal mapping of the synthesized $\text{Er}^{3+}/\text{TiO}_2$ NPs.

3.3. Energy Gaps

The absorbance spectra of the synthesized NPs samples were obtained at room temperature and are illustrated in Figure 5. A significant absorption peak in the UV–Vis spectrum is located at 320 nm. According to Equation (6), the energy gaps for the synthesized samples of NPs were calculated:

$$\alpha h\nu = E_d(h\nu - E_g)^{\frac{1}{2}} \quad (6)$$

where α represents the optical coefficient; h refers to the Planck constant; the multiplication of $h\nu$ represents the photon energy; E_g and E_d represent the energy gap and a constant, respectively [40]. ($\alpha h\nu$) versus $h\nu$ was drawn, the linear section of the curve was extrapolated, and E_g was evaluated, as shown in Figure 6. The E_g values of TiO_2 NPs for different weight percentages of Er ions are given in Table 4. The lowest energy gap value obtained was 2.63 eV for Er ions/titanium dioxide NPs.

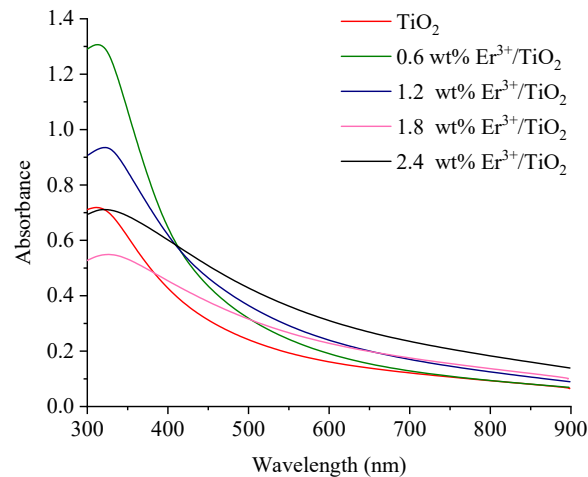


Figure 5. Ultraviolet–visible spectra of the synthesized NPs.

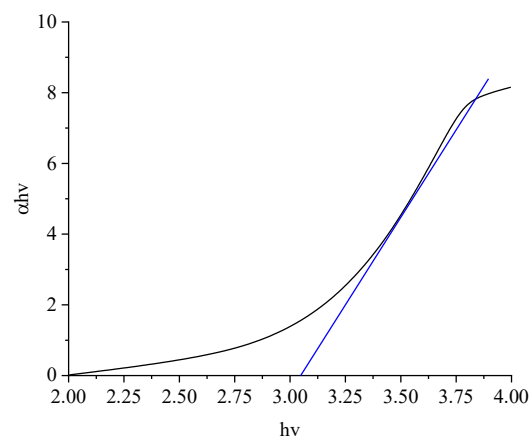


Figure 6. Calculation of the direct band gap energy obtained in our study.

Table 4. Energy gaps for the synthesized $\text{Er}^{3+}/\text{TiO}_2$ NP samples.

$\text{Er}^{3+}/\text{TiO}_2$ (wt %)	Energy Gap (eV)
TiO_2	3.13 ± 0.02
0.6	3.20 ± 0.02
1.2	3.00 ± 0.02
1.8	2.63 ± 0.02
2.4	2.70 ± 0.02

3.4. Application as a Blue-Wavelength-Blocking Contact Lens

Given most people's modern lifestyles, they spend the majority of their waking hours staring at digital devices. According to the previous studies, 60% of people spend 6–7 h per day looking directly at digital screens [41,42]. Digital screens, sunlight, electronics, and fluorescent light sources emit a blue wavelength ranging from 300 to 500 nm. This range is harmful to the eye (damages the retinal photoreceptors and destroys the crystalline lens protein that appears as a white cloud) [43].

The human eye's natural filters do not protect the eye's components against these highest-energy wavelengths. The excessive exposure to blue light rays may affect the retinal tissues and cause damage. This contributes to age-related macular degradation and subsequent loss of vision. In this work, 0.6% wt/vol $\text{Er}^{3+}/\text{TiO}_2$ solution drops were spin-coated on a previously prepared poly(methyl methacrylate)—titanium dioxide (PMMA- TiO_2) contact lens fixed on a convex glass mold (Figure 7a) [11]. The refractive index was measured using an Abbe Refractometer at wavelengths of 486.1, 587.6, and 656.3 nm as 1.509, 1.503, and 1.499, respectively. The Abbe number was calculated as 52.35 using the following equation [44]:

$$v_d = \frac{(n_d - 1)}{(n_f - n_c)} \quad (7)$$

where v_d is the Abbe number; and n_c , n_d , and n_f are refractive indices of the polymer films at wavelengths of 656, 589, and 486 nm, respectively.

From the results provided above, it can be found that the fabricated coated contact lens works in the acceptable physical range according to the refractive index, which is near the refractive indices of the eye tissues. The resulting contact lens was modeled using ZEMAX optical design software (version 14) to evaluate the blue-wavelength-blocking characteristics before conducting an in vivo study. The Liou and Brennan eye model was chosen in this study because it was experimentally obtained from the human eye [45]. The $\text{Er}^{3+}/\text{TiO}_2$ coating worked as a blue wavelength filter, where it prevented the wavelength range of 0.45–0.47 nm from being transmitted (reduced the light transmittance to 0%) through the contact lens, as illustrated in Figure 7c.

The $\text{Er}^{3+}/\text{TiO}_2$ coating does not degrade the retinal image's clarity, as shown in Figure 8. To compare the retinal image before and after coating, image simulation was used for evaluation. A polychromatic light source was applied to the modeled eye, a perfect eye with a high retinal image contrast, and sharpness was obtained by the eye with the PMMA- TiO_2 contact lens with no aberrations, as shown in Figure 8a. After, the resultant PMMA- TiO_2 contact lens coated with $\text{Er}^{3+}/\text{TiO}_2$ layer was fitted on the modeled eye, and the image at the retina showed high clarity and no indication of aberration generation. This indicates that the coated lens focused the rays entering the eye in one small spot, which is the focal point. This performance was obtained due to n value of the resulting lens and the dispersion factor, which is able to maintain image clarity under polychromatic light illumination. The speed of each component of white light differs from the speed of the other wavelengths according to the concept of the refractive index ($n = c/v$). The blocking lens color is suitable and not too deep, so it prevents color deviation and darkness. The designed contact lens can work as a filter or polarizer, blocking the reflected blue portion of light from the object and passing the other components of the light through to the eye. From observing the sharpness and contrast of the two images before and after the application of the coating, we found the coating does not affect the visual function of the eye.

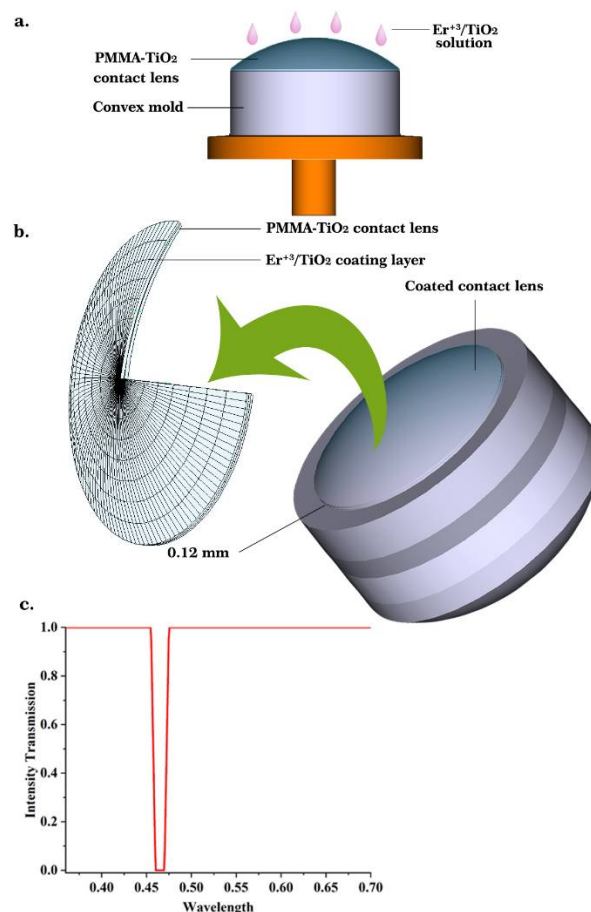


Figure 7. (a) Spin-coating a contact lens with 0.6 wt/vol % $\text{Er}^{3+}/\text{TiO}_2$ solution; (b) The layers of the resulting contact lens; (c) intensity transmission as a function of wavelength blocking 0.45–0.47 nm from transmission.

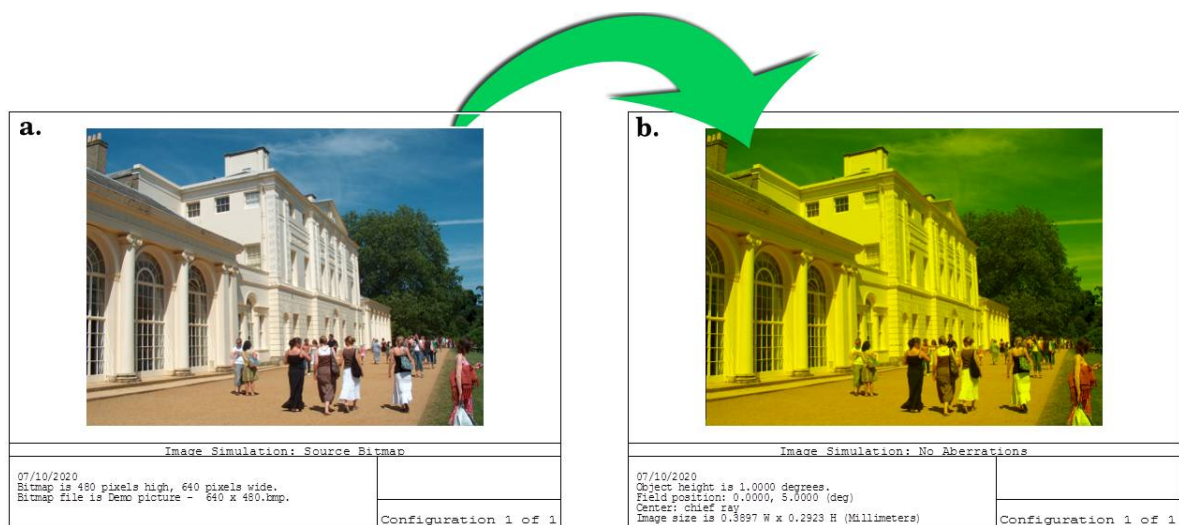


Figure 8. (a) The retinal image resulting from the eye with a PMMA-TiO₂ contact lens; (b) the retinal image resulting from the eye with a PMMA-TiO₂ contact lens coated with Er³⁺/TiO₂ NPs.

4. Conclusions

Titanium dioxide NPs were impregnated with different weight percentages of *Er* ions using the impregnation technique and then calcination of the product at 500 °C. The Er³⁺/TiO₂ NPs showed an energy gap decrease with increasing *Er* ions weights percent up to 1.8 wt %. Agglomeration and particle size increased with increasing *Er* ions weight percent. Relative to the long hours people spend staring at digital displays, researchers are developing eyeglass lenses that partially filter the high-energy blue wavelength. Due to the problems with glasses such as their weight, the possibility of breaking them, amongst others, we attempted to design and manufacture a contact lens with a high *n* value that works as a filter to reduce the transmission of blue light intensity without affecting the clarity of the image. The fabricated spin-coated Er³⁺/TiO₂ layer on the PMMA-TiO₂ contact lens works as a filter as it absorbs the high-energy blue wavelength and passes other components of light through to the eye. A perfect polarized retinal image was achieved, and no aberration was generated.

Author Contributions: Conceptualization, A.A. and L.M.S.; methodology, A.A. and L.M.S. software, L.M.S.; validation, W.N.R.W.I. and M.T.; formal analysis, L.M.S.; investigation, A.A. and L.M.S.; resources, W.N.R.W.I. and M.T.; data curation, L.M.S.; writing—original draft preparation, A.A. and L.M.S.; writing—review and editing, A.A.; visualization, M.T.; supervision, A.A., W.N.R.W.I. and M.T.; project administration, A.A., W.N.R.W.I. and M.T.; funding acquisition, W.N.R.W.I. and M.T. All authors have read and agreed to the published version of the manuscript.

Funding: This research was funded by Universiti Kebangsaan Malaysia under grant GUP2020-012.

Institutional Review Board Statement: Not applicable.

Informed Consent Statement: Not applicable.

Data Availability Statement: The data of this study are available from the corresponding author (A.A.), upon reasonable request.

Acknowledgments: The authors thank Universiti Kebangsaan Malaysia (Malaysia) and University of Technology (Iraq) for supporting this work.

Conflicts of Interest: The authors declare no conflict of interest.

References

1. Lindenthal, L.; Raffael, R.; Harald, S.; Thomas, R.; Janko, P.; Andreas, N.; Stefan, L.; Alexander, K.O.; Peter, B.; Christoph, R. Modifying the Surface Structure of Perovskite-Based Catalysts by Nanoparticle Exsolution. *Catalysts* **2020**, *10*, 268. [[CrossRef](#)]
2. Abdel-Khalek, N.A.; Abdel-Khalek, M.A.D.; Selim, K.A.; Abdullah, S.S. Physicochemical study and application for pyrolusite separation from high manganese-iron ore in the presence of microorganisms. *Physicochem. Probl. Miner. Process.* **2021**, *57*, 273–283.
3. Ahmad, H.; Kamarudin, S.K.; Minggu, L.J.; Hasran, U.A.; Masdar, S.; Daud, W.R.W. Enhancing methanol oxidation with a TiO₂-modified semiconductor as a photo-catalyst. *Int. J. Hydrog. Energy* **2017**, *42*, 8986–8996. [[CrossRef](#)]
4. Wasmı, B.; Al-Amıery, A.A.; Kadhıum, A.A.H.; Takrıff, M.S.; Mohamad, A.B. Synthesis of vanadium pentoxide nanoparticles as catalysts for the ozonation of palm oil. *Ozone Sci. Eng.* **2016**, *38*, 36–41. [[CrossRef](#)]
5. Zheng, M.; Wang, Y.; Feng, P. Bifunctional heterometallic metal-organic frameworks for solvent-free heterogeneous cascade catalysis. *Catalysts* **2020**, *10*, 309. [[CrossRef](#)]
6. Sandu, M.P.; Sidelnikov, V.S.; Geraskin, A.A.; Chernyavskii, A.V.; Kurzina, I.A. Influence of the method of preparation of the Pd-Bi/Al₂O₃ catalyst on catalytic properties in the reaction of liquid-phase oxidation of glucose into gluconic acid. *Catalysts* **2020**, *10*, 271. [[CrossRef](#)]
7. Yu, H.; Song, L.; Hao, Y.; Lu, N.; Quan, X.; Chen, S.; Zhang, Y.; Feng, Y. Fabrication of pilot-scale photocatalytic disinfection device by installing TiO₂ coated helical support into UV annular reactor for strengthening sterilization. *Chem. Eng. J.* **2016**, *283*, 1506–1513. [[CrossRef](#)]
8. Wang, F.; Zhang, H.; Yu, B.; Wang, S.; Shen, Y.; Cong, H. Review of the research on anti-protein fouling coatings materials. *Prog. Org. Coat.* **2020**, *147*, 105860. [[CrossRef](#)]
9. Melgoza-Ramírez, M.L.; Ramírez-Bon, R. Europium ions as a spectroscopic probe in the study of PMMA-SiO₂ hybrid microstructure with variable coupling agent. *J. Sol-Gel Sci. Technol.* **2021**, *99*, 1–11.
10. Shaker, L.M.; Al-Amıery, A.A.; Kadhıum, A.A.H.; Takrıff, M.S. Manufacture of Contact Lens of Nanoparticle-Doped Polymer Complemented with ZEMAX. *Nanomaterials* **2020**, *10*, 2028. [[CrossRef](#)] [[PubMed](#)]
11. Harb, S.V.; Bassous, N.J.; de Souza, T.A.; Trentin, A.; Pulcinelli, S.H.; Santilli, C.V.; Webster, T.J.; Lobo, A.O.; Hammer, P. Hydroxyapatite and β-TCP modified PMMA-TiO₂ and PMMA-ZrO₂ coatings for bioactive corrosion protection of Ti6Al4V implants. *Mater. Sci. Eng. C* **2020**, *116*, 111149. [[CrossRef](#)]
12. Savchyn, V.P.; Popov, A.I.; Aksimentyeva, O.I.; Klym, H.; Horbenko, Y.Y.; Serga, V.; Moskina, A.; Karbovnyk, I. Cathodoluminescence characterization of polystyrene-BaZrO₃ hybrid composites. *Low Temp. Phys.* **2016**, *42*, 597–600. [[CrossRef](#)]
13. Aksimentyeva, O.I.; Savchyn, V.P.; Dyakonov, V.P.; Piechota, S.; Horbenko, Y.Y.; Opainych, I.Y.; Demchenko, P.Y.; Popov, A.; Szymczak, H. Modification of polymer-magnetic nanoparticles by luminescent and conducting substances. *Mol. Cryst. Liq. Cryst.* **2014**, *590*, 35–42. [[CrossRef](#)]
14. Li, F.; Kong, W.; Bhushan, B.; Zhao, X.; Pan, Y. Ultraviolet-driven switchable superliquiphobic/superliquiphilic coating for separation of oil-water mixtures and emulsions and water purification. *J. Colloid Interface Sci.* **2019**, *557*, 395–407. [[CrossRef](#)]
15. Umar, A.A.; Saad, S.K.M.; Umar, M.I.A.; Abd Rahman, M.Y.; Oyama, M. Advances in porous and high-energy (001)-faceted anatase TiO₂ nanostructures. *Opt. Mater.* **2018**, *75*, 390–430. [[CrossRef](#)]
16. Li, X.Z.; Li, F.B. Study of Au/Au³⁺-TiO₂ photocatalysts toward visible photooxidation for water and wastewater treatment. *Environ. Sci. Technol.* **2001**, *35*, 2381–2387. [[CrossRef](#)]
17. Manassero, A.; Satuf, M.L.; Alfano, O.M. Evaluation of UV and visible light activity of TiO₂ catalysts for water remediation. *Chem. Eng. J.* **2013**, *225*, 378–386. [[CrossRef](#)]
18. Hoffmann, M.R.; Martin, S.T.; Choi, W.; Bahnemann, D.W. Environmental Applications of Semiconductor Photocatalysis. *Chem. Rev.* **1995**, *95*, 69–96. [[CrossRef](#)]
19. Liqiang, J.; Yichun, Q.; Baiqi, W.; Shudan, L.; Baojiang, J.; Libin, Y.; Wei, F.; Honggang, F.; Jiazhong, S. Review of Photoluminescence Performance of Nano-Sized Semiconductor Materials and Its Relationships with Photocatalytic Activity. *Sol. Energ. Mater. Sol. Cells* **2006**, *90*, 1773–1787. [[CrossRef](#)]
20. Linsebigler, A.; Lu, G.; Yates, J.T. Photocatalysis on TiO₂ Surfaces: Principles, Mechanisms, and Selected Results. *Chem. Rev.* **1995**, *95*, 735–758. [[CrossRef](#)]
21. Li, H.; Bian, Z.; Zhu, J.; Huo, Y.; Li, H.; Lu, Y. Mesoporous Au/TiO₂ Nanocomposites with Enhanced Photocatalytic Activity. *J. Am. Chem. Soc.* **2007**, *129*, 4538–4539. [[CrossRef](#)] [[PubMed](#)]
22. Zaleska, A. Doped-TiO₂: A Review. *Recent Pat. Eng.* **2008**, *2*, 157–164. [[CrossRef](#)]
23. Di Paola, A.; Marcı, G.; Palmisano, L.; Schiavello, M.; Uosaki, K.; Ikeda, S.; Ohtani, B. Preparation of Polycrystalline TiO₂ Photocatalysts Impregnated with Various Transition Metal Ions: Characterization and Photocatalytic Activity for the Degradation of 4-Nitrophenol. *J. Phys. Chem. B* **2002**, *106*, 637–645. [[CrossRef](#)]
24. Sakthivel, S.; Shankar, M.V.; Palanichamy, M.; Arabindoo, B.; Bahnemann, D.W.; Murugesan, V. Enhancement of Photocatalytic Activity by Metal Deposition: Characterization and Photonic Efficiency of Pt, Au and Pd Deposited on TiO₂ Catalyst. *Water Res.* **2004**, *38*, 3001–3008. [[CrossRef](#)]
25. Chen, X.; Mao, S.S. Titanium Dioxide Nanomaterials: Synthesis, Properties, Modifications, and Applications. *Chem. Rev.* **2007**, *107*, 2891–2959. [[CrossRef](#)]
26. Ohtani, B.; Iwai, K.; Nishimoto, S.; Sato, S. Role of Platinum Deposits on Titanium(IV) Oxide Particles: Structural and Kinetic Analyses of Photocatalytic Reaction in Aqueous Alcohol and Amino Acid Solutions. *J. Phys. Chem. B* **1997**, *101*, 3349–3359. [[CrossRef](#)]

27. Ibhaddon, A.O.; Fitzpatrick, P. Heterogeneous photocatalysis: Recent advances and applications. *Catalysts* **2013**, *3*, 189–218. [[CrossRef](#)]
28. Estrellan, C.R.; Salim, C.; Hinode, H. Photocatalytic activity of sol–gel derived TiO₂ Co-doped with iron and niobium. *React. Kinet. Catal. Lett.* **2009**, *98*, 187–192. [[CrossRef](#)]
29. Yu, C.L.; Yang, K.; Yu, J.; Peng, P.; Cao, F.; Li, X.; Zhou, X.C. Effects of rare earth Ce doping on the structure and photocatalytic performance of ZnO. *Acta Phys. Chim. Sin.* **2011**, *27*, 505–512.
30. Minero, C.; Pelizzatti, E.; Sega, M.; Friberg, S.E.; Sjoblom, J. The role of humic substances in photocatalytic degradation of water contaminants. *J. Dispers. Sci. Technol.* **1999**, *20*, 643–661. [[CrossRef](#)]
31. Mohammad, G.; Mohammed, W.; Marzoug, T.R.; Al-Amiery, A.; Kadhum, A.; Mohamad, A. Green synthesis, antimicrobial and cytotoxic effects of silver nanoparticles using Eucalyptus chapmaniana leaves extract. *Asian Pac. J. Trop. Biomed.* **2013**, *3*, 58–63.
32. Gaaz, T.S.; Sulong, A.B.; Kadhum, A.A.H.K.; Nassir, M.H.; Al-Amiery, A.A. Impact of sulfuric acid treatment of halloysite on physico-chemic property modification. *Materials* **2016**, *9*, 620. [[CrossRef](#)]
33. Gaaz, T.S.; Sulong, A.B.; Akhtar, M.N.; Kadhum, A.A.H.; Mohamad, A.B.; Al-Amiery, A.A. Properties and applications of polyvinyl alcohol, halloysite nanotubes and their nanocomposites. *Molecules* **2015**, *20*, 22833–22847. [[CrossRef](#)]
34. Obayes, H.; Al-Gebori, A.; Khazaaal, S.; Jarad, A.; Alwan, G.; Al-Amiery, A. Hypothetical design of carbon nanotube materials based on [8] circulene. *J. Nanoelectron. Optoelectron.* **2015**, *10*, 711–716. [[CrossRef](#)]
35. Wasmı, W.; Al-Amiery, A.; Kadhum, A.; Mohamad, A. Novel approach: Tungsten oxide nanoparticle as a catalyst for malonic acid ester synthesis via ozonolysis. *J. Nanomater.* **2014**, *2014*, 1–7. [[CrossRef](#)]
36. Serga, V.; Burve, R.; Krumina, A.; Romanova, M.; Kotomin, E.A.; Popov, A.I. Extraction–Pyrolytic Method for TiO₂ Polymorphs Production. *Crystals* **2021**, *11*, 431. [[CrossRef](#)]
37. Tsebriienko, T.; Popov, A.I. Effect of Poly(Titanium Oxide) on the Viscoelastic and Thermophysical Properties of Interpenetrating Polymer Networks. *Crystals* **2021**, *11*, 794. [[CrossRef](#)]
38. Serga, V.; Burve, R.; Krumina, A.; Pankratova, V.; Popov, A.I.; Pankratov, V. Study of phase composition, photocatalytic activity, and photoluminescence of TiO₂ with Eu additive produced by the extraction-pyrolytic method. *J. Mater. Res. Technol.* **2021**, *13*, 2350–2360. [[CrossRef](#)]
39. Dahl, M.; Liu, Y.; Yin, Y. Composite titanium dioxide nanomaterials. *Chem. Rev.* **2014**, *114*, 9853–9889. [[CrossRef](#)]
40. Vijayalakshmi, R.; Rajendran, V. Synthesis and characterization of nano-TiO₂ via different methods. *Arch. Appl. Sci. Res.* **2012**, *4*, 1183–1190.
41. Rohatgi, S.; Hanna, T.N.; Sliker, C.W.; Abbott, R.M.; Nicola, R. After-hours radiology: Challenges and strategies for the radiologist. *Am. J. Roentgenol.* **2015**, *205*, 956–961. [[CrossRef](#)] [[PubMed](#)]
42. Waite, S.; Kolla, S.; Jeudy, J.; Legasto, A.; Macknik, S.L.; Martinez-Conde, S.; Krupinski, E.A.; Reede, D.L. Tired in the reading room: The influence of fatigue in radiology. *J. Am. Coll. Radiol.* **2017**, *14*, 191–197. [[CrossRef](#)]
43. Michael, R.; Wegener, A. Estimation of safe exposure time from an ophthalmic operating microscope with regard to ultraviolet radiation and blue-light hazards to the eye. *J. Opt. Soc. Am. A* **2004**, *21*, 1388–1392. [[CrossRef](#)] [[PubMed](#)]
44. Michael, A.S.; Schwiegerling, J.; Fest, E.; Hamilton, R. *Visual Optics, in Molded Optics: Design and Manufacture*; CRC Press: Boca Raton, FL, USA, 2016; pp. 2–58.
45. Brennan, N.A.; Liou, H.-L. Anatomically accurate, finite model eye for optical modeling. *Opt. Soc. Am.* **1997**, *14*, 1684–1695.